Nonequilibrium Capillary Pressure and Relative Permeability Curves of Porous Media

C. D. Tsakiroglou, M. A. Theodoropoulou and V. Karoutsos
Institute of Chemical Engineering and High Temperature Chemical Processes—Foundation for Research and
Technology Hellas, Stadiou St., Platani, GR-26504 Patras, Greece

History matching of unsteady immiscible displacement experiments performed on model porous media reveals that nonequilibrium capillary pressure and relative permeability functions are sensitive to the dominating flow pattern. As the capillary number increases, the network displacement pattern changes gradually from invasion percolation cluster to stable displacement. For primary drainage, the capillary pressure and relative permeability curves are increasing functions of the capillary number. The dependence of the relevant macroscopic parameters on the capillary number is consistent with power laws derived from scaling arguments of gradient percolation theory, which describes the growth of the displacement front. The material coefficient of the thermodynamic theory of capillary pressure changes mildly with fluid saturation and is a decreasing function of the capillary number.

Introduction

Two-phase flow in porous media is of key importance for a variety of industrial (such as oil and gas recovery from underground reservoirs) and environmental (such as remediation of contaminated soils and aquifers, CO_2 storage in sub-sea aquifers, and so on) processes. At the macroscopic scale, the multifluid flow in porous media is commonly described by the Darcy equation and the continuity equation for each phase (Bear, 1972; Sahimi, 1995). The capillary pressure and relative permeability curves incorporate implicitly microscopic characteristics of the porous medium and pore-scale dynamics into the macroscopic description of the flow, and are commonly expressed as functions of the local fluid saturation (Scheidegger, 1974).

Experiments performed on artificial porous media (Lenormand et al., 1988; Vizika and Payatakes, 1989; Fourar et al., 1993; Avraam and Payatakes, 1995a; Persoff and Pruess, 1995), as well as pore network simulations (Blunt and King, 1991; Goode and Ramakrishnan, 1993; Vizika et al., 1994; Constantinides and Payatakes, 1996; Aker et al., 1998; Hughes and Blunt, 2000; Knackstedt et al., 2001; Singh and Mohanty, 2003), have revealed that the transient and steady-state two-phase flow patterns depend not only on the specific characteristics of the pore space morphology, but also on a variety of dimensionless parameters such as the capillary number, viscosity ratio, wettability, and so on. The relative permeability functions of porous media are strongly correlated with the flow regimes and are strongly dependent on the capillary number and viscosity ratio, not only over the inertial (Fourar et al., 1993), but also over the creeping flow regime (Avraam and Payatakes, 1995a; Singh et al., 2001). The extension of Darcy law to two-phase flows is based on the assumption that each phase flows along its own pathway without any momentum interchange between phases at interfaces (Whitaker, 1986). The viscous coupling effects are accounted for the two-phase flow by substituting the conventional Darcy equations with the generalized ones along with four relative permeability coefficients (Kalaydjian, 1990; Bentsen and Manai, 1993; Avraam and Payatakes, 1995b; Dullien and Dong, 1996).

At vanishing flow rates, the displacement is driven by capillary forces, the relative permeability and capillary pressure curves are governed by the microstructural properties and wettability of the porous medium and various numerical models have been suggested for their calculation by using either invasion percolation or effective medium approximation (Blunt et al., 1992; Kantzas and Chatzis, 1988; Levine and Cuthiel, 1986). For drainage or imbibition in a disordered pore network, at increasing values of the capillary number, the correlation length (Stauffer and Aharony, 1992) de-

---

Correspondence concerning this article should be addressed to C. D. Tsakiroglou.

creases and viscous effects on the growth pattern of the displacement become discernible in progressively smaller regions of the network. Near the percolation threshold of any fluid, this picture is analogous with the substitution of an infinite network by smaller finite networks. Then, finite-size scaling of the various percolation quantities at the vicinity of the percolation threshold allows the estimation of the shift of the network accessibility properties and effective conductivities with respect to the capillary number (Wilkinson, 1986; Blunt et al., 1992; Xu et al., 1998).

From the analysis of literature experiments and simulated results of pore network models with the aid of the thermodynamic theory of the two-phase flow in porous media (Hassanizadeh and Gray, 1993a,b; Hassanizadeh et al., 2002), it was found out that the functional form of the capillary pressure curve should be generalized to include a dynamic term (material coefficient), which may be of crucial importance for obtaining reliable numerical predictions at the field scale. Specifically, drainage experiments indicate that the dynamic capillary pressure is almost always higher than the static one, and comparative analysis of experimental data allows the estimation of the material coefficient (Hassanizadeh et al., 2002).

The estimation of relative permeability and capillary pressure functions from laboratory measurements may be based on steady-state experiments of the simultaneous flow of two phases through the porous medium or unsteady-state experiments of the immiscible displacement of the one fluid by the other (Heaviside, 1991). Although accurate and explicit, the steady-state methods are time consuming and expensive. On the other hand, in the unsteady-state methods, the effective transport coefficients are estimated either explicitly from measured data (Johnson et al., 1959) or implicitly from the history-matching of the temporal evolution of the pressure drop/fluid production/fluid saturation profile (Sigmund and McCaffrey, 1979; Jennings et al., 1988; Chardaire-Riviere et al., 1992; Mejia et al., 1995; Kulkarni et al., 1998; Mitlin et al., 1999; Akin, 2001). The accuracy of the explicit unsteady-state methods is limited by errors arising from the calculation of derivatives (Tao and Watson, 1984). In implicit methods, the capillary pressure and relative permeability functions are so chosen that simulated results match the experimental data (Watson et al., 1986). Common difficulties embedded in history-matching procedures are associated with the adequacy of the numerical model of the displacement process, as well as with the selection of an optimization scheme that will be capable of finding a global minimum of parameter estimates (Savioli and Bidner, 1994). Except for the classical nonlinear parameter estimation methods (Bard, 1974), simulated annealing and genetic algorithms have also been used as optimization tools in reservoir engineering (Johnson and Rogers, 2001; Akin and Demiral, 1998).

Although it is well known that the transient displacement patterns in a porous medium are strongly correlated with the capillary number, the dependence of the implicitly estimated multiphase flow coefficients (history matching) on the flow rates has been overlooked. However, the introduction of incorrect parameters into the macroscopic numerical simulators is reflected in inaccurate predictions of the multifluid transport at the scale of an oil reservoir or an underground aquifer. In this manner, the financial risk of decisions concerning the management of oil and gas reservoirs or the remediation of oil-contaminated aquifers increases. On the other hand, the performance of displacement tests on cores, at several flow rates, increases the cost of laboratory analyses. Therefore, there is a need for methods that will enable the engineer to select the most suitable parameters for capillary pressure and relative permeability functions based on the flow conditions prevailing in the investigated problem, and a representative number of displacement core tests.

Table 1. Physicochemical Properties of Fluid System

Water viscosity, μ_w (Pa·s)	0.001
Paraffin oil viscosity, μ_{nw} (Pa·s)	0.026
Water/oil interfacial tension, γ (Nt/m)	35 10^{-3}

Static contact angle, ω(°) 41.

In the present work, unsteady displacement experiments, performed on a transparent glass-etched planar pore network at varying values of the capillary number, are utilized to estimate the relative permeability and capillary pressure functions in dependence on the capillary number. The experimentally measured transient changes of the NWP saturation, distribution of NWP saturation along the porous medium and total pressure drop across it are introduced into an appropriate nonlinear parameter estimation numerical scheme developed in the environment of the commercial software package ATHENA. Scaling arguments of the gradient percolation theory are used to correlate the estimated macroscopic parameters with capillary number. Finally, experimental data and estimated parameter values of capillary pressure are used for the determination of the material coefficient of the macroscopic thermodynamic theory.

Materials and Methods

Distilled water colored with methylene blue and paraffin oil were selected as the wetting (WP) and nonwetting phase (NWP), respectively (Table 1). A large planar pore network, etched on glass with photo-lithographic techniques was used as the model porous medium (Table 2). Experiments were performed at a constant ratio of NWP viscosity to WP viscosity, $\kappa = 26$, and five values of the capillary number Ca, shown in Table 3. Definition of the various capillary numbers is given in detail in Appendix A.

Details about the morphology of the artificial model (Figure 1b) and the procedure followed for performing two-phase flow experiments on it (Figure 1a) are reported in Theodor-

Table 2. Properties of the Model Porous Medium

Topology	2-D square lattice
Length × Width, $L_T \times W_T$ (cm × cm)	13.4 × 10.3
*Areal porosity, φ_A	0.35
Cross-sectional porosity, φ	0.025
Length of central region, L (cm)	6.85
Pore cross-sectional shape	Elliptical
Mean pore depth, $\langle D_P \rangle$ (μm)	126
Mean pore width, $\langle W_P \rangle$ (μm)	470
Pore length, L_P (μm)	1,365
Absolute permeability, k (Da)	20.5

*For a 2-D porous medium it is defined as the fraction of the total area occupied by pores.

Table 3. Experimental Conditions

Capillary number, Ca	Average retention time, t_r (s)
6.55×10^{-8}	32130
1.31×10^{-7}	16110
1.31×10^{-6}	1611
6.55×10^{-6}	322
1.31×10^{-5}	161

opoulou et al. (2001). First, the network becomes completely saturated with the WP, and then, the NWP is injected in the network through its inlet ports at a pre-selected flow rate, using an infusion-withdrawal pump (Figure 1a). Successive short-cuts of the displacement are captured from a central region of the network (Figure 1b) with a CCD video-camera and are recorded on the hard-disk through an image grabber installed in the host computer (Figure 1a).

The pressure drop along the central region (viewed area) of the pore network is measured with a differential pressure transducer and is transmitted to a data acquisition card installed in the host PC (Figure 1a), where it is recorded at constant time intervals ranging from ~ 1 s for the fastest to ~ 1 min for the slowest experiment. At the end of experiments, the transient response of the pressure drop is smoothed out by fitting a 10th-order polynomial to the measurements (Figure 2). Note that the time $t = 0$ s corresponds to the instant that the NWP enters the central region of the network, while negative times refer to the earlier period during which the NWP invades the entrance region of the network.

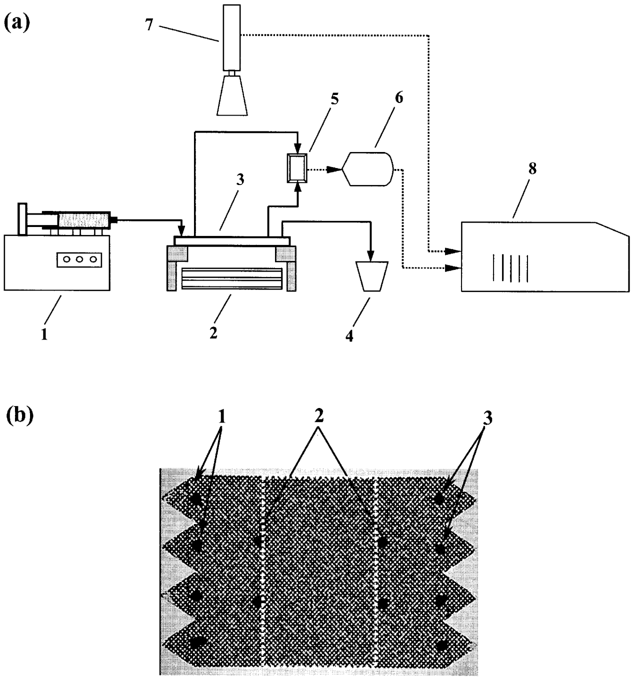

Figure 1. (a) Experimental apparatus; (b) overview of glass micromodel.

(a): 1 = Syringe pump; 2 = light source; 3 = glass micromodel; 4 = waste storage tank; 5 = differential pressure transducer; 6 = pressure display; 7 = video-camera with zoom-lens; 8 = host computer. (b): 1 = inlet ports; 2 = pressure taps; 3 = outlet ports; the dotted lines indicate the bounds of the central region of the network.

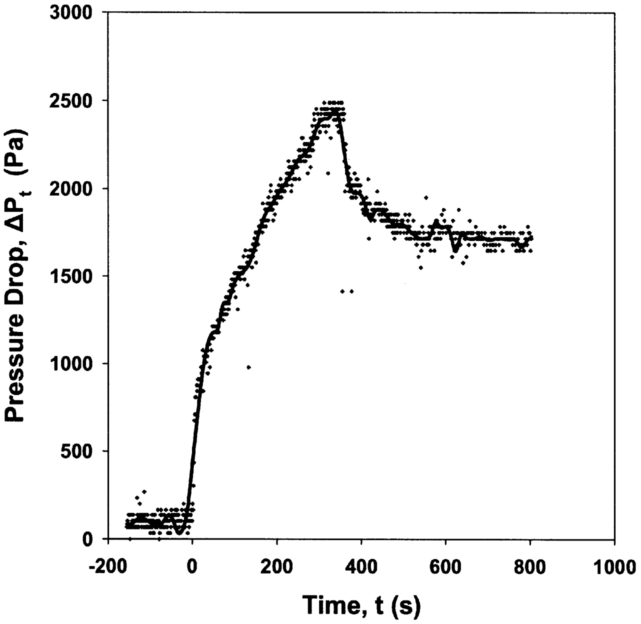

Figure 2. Measured time response of the pressure drop along the central region of the pore network for $Ca = 6.5\times10^{-6}$.

The NWP saturation in the network $S_{nwt}(t)$ is determined as a function of time by digitizing each image and measuring the percentage of the network area occupied by the NWP phase with the aid of the Sigma Scan Pro 5.0 software package. Except for the total NWP saturation, the distribution of NWP saturation along the pore network is also determined by sectioning its central region into seven slices of finite and equal thickness and measuring the NWP saturation in each slice, $S_{nws}(t,x_m)$ (Figure 3). The two data sets are measured separately and with a different length of resolution (Figure 3), so that independence of the experimental errors embedded into each set of measurements is ensured.

Estimation of Capillary Pressure and Relative Permeability Functions

Mathematical models

The one-dimensional (1-D) and horizontal (no gravity) flow of two incompressible fluids in a homogeneous and isotropic porous medium is described by the averaged mass (continuity equation) and momentum (Darcy equation) balances, written for each phase, namely

$$\varphi\frac{\partial S_i}{\partial t} + \frac{\partial u_i}{\partial x} = 0 \tag{1}$$

$$u_i = -\frac{kk_{ri}}{\mu_i}\frac{\partial P_i}{\partial x} \tag{2}$$

In the foregoing equations, the index i refers either to the wetting ($i = w$) or to the nonwetting ($i = nw$) fluid, μ_i, u_i, P_i,

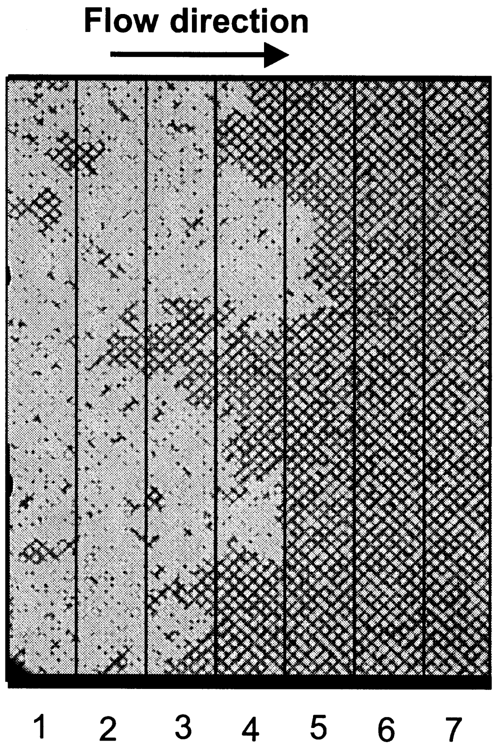

Figure 3. Shortcut of the displacement of WP (dark) by NWP (white) for $Ca = 1.3 \times 10^{-7}$ at time $t = 103$ min.

Measured total NWP saturation: $S_{nwt} = 0.37$. Measured NWP saturation in each slice: $S_{nws}(1) = 0.804$, $S_{nws}(2) = 0.7$, $S_{nws}(3) = 0.35$, $S_{nws}(4) = 0.117$, $S_{nws}(5) = 0.017$, $S_{nws}(6) = 0.0$, $S_{nws}(7) = 0.0$.

S_i are the dynamic viscosity, (average) superficial velocity, pressure, saturation of phase i, k_{ri} is the relative permeability of phase i at saturation S_i, φ and k are the porosity and absolute permeability of the medium, t is the time, and x is the axial coordinate. Moreover, the capillary pressure is defined as the difference between the local pressures of the two fluids and is written as

$$P_c = P_{nw} - P_w \tag{3}$$

whereas the fluid saturations are interrelated by

$$S_w + S_{nw} = 1.0 \tag{4}$$

By defining the fractional flow F_{nw} as the ratio of the local NWP velocity u_{nw} to the total velocity u_0, namely

$$F_{nw} = \frac{u_{nw}}{u_0} \qquad 0 \le F_{nw} \le 1.0 \tag{5}$$

and using the dimensionless variables

$$\xi = \frac{x}{L} \quad \text{and} \quad \tau = \frac{u_0 t}{\varphi L} \tag{6}$$

Equations 1–4 result in

$$\frac{\partial S_{nw}}{\partial \tau} + \frac{\partial F_{nw}}{\partial \xi} = 0 \tag{7}$$

$$F_{nw} = \frac{k_{rnw}}{\kappa k_{rw} + k_{rnw}} \left[1 - \frac{u_c}{u_0} k_{rw} \frac{\partial P_c^*}{\partial \xi} \right] \tag{8}$$

where κ is the viscosity ratio given by

$$\kappa = \frac{\mu_{nw}}{\mu_w} \tag{9}$$

P_c^* is a dimensionless capillary pressure, defined by

$$P_c^* = \frac{P_c}{\Delta P_{nw}^0} \tag{10}$$

ΔP_{nw}^0 is the experimentally measured pressure drop along the NWP at steady state ($t \to \infty$), u_c is a characteristic superficial velocity defined by

$$u_c = \frac{k \Delta P_{nw}^0}{\mu_w L} \tag{11}$$

and L is the length of the porous medium. The capillary pressure and relative permeabilities may be regarded as parametric functions of the NWP saturation, namely, $P_c = P_c(S_{nw};\boldsymbol{\theta})$, $k_{rw} = k_{rw}(S_{nw};\boldsymbol{\theta})$, $k_{rnw} = k_{rnw}(S_{nw};\boldsymbol{\theta})$, where $\boldsymbol{\theta}$ is the vector of unknown parameters. By substituting, Eq. 8 to Eq. 7 and, after some manipulation, we get

$$\frac{\partial S_{nw}}{\partial \tau} + A_1 \frac{\partial S_{nw}}{\partial \xi} - (A_1 A_2 + B_1 + B_2) \left(\frac{\partial S_{nw}}{\partial \xi} \right)^2 - B_3 \frac{\partial^2 S_{nw}}{\partial \xi^2} = 0 \tag{12}$$

where

$$A_1 = \frac{\kappa \left(k_{rw} \frac{\partial k_{rnw}}{\partial S_{nw}} - k_{rnw} \frac{\partial k_{rw}}{\partial S_{nw}} \right)}{(\kappa k_{rw} + k_{rnw})^2} \tag{13}$$

$$A_2 = \left(\frac{u_c}{u_0} \right) k_{rw} \frac{\partial P_c^*}{\partial S_{nw}} \tag{14}$$

$$B_1 = \left(\frac{u_c}{u_0} \right) \frac{k_{rnw}}{\kappa k_{rw} + k_{rnw}} \frac{\partial k_{rw}}{\partial S_{nw}} \frac{\partial P_c^*}{\partial S_{nw}} \tag{15}$$

$$B_2 = \left(\frac{u_c}{u_0} \right) \frac{k_{rnw} k_{rw}}{\kappa k_{rw} + k_{rnw}} \frac{\partial^2 P_c^*}{\partial S_{nw}^2} \tag{16}$$

$$B_3 = \left(\frac{u_c}{u_0} \right) \frac{k_{rnw} k_{rw}}{\kappa k_{rw} + k_{rnw}} \frac{\partial P_c^*}{\partial S_{nw}} \tag{17}$$

Equation 12 is a nonlinear parabolic differential equation that is subject to the initial condition

$$S_{nw}(0,\xi) = 0 \tag{18}$$

and boundary conditions

$$S_{nw}(\tau,0) = 1 - S_{wi} \tag{19}$$

$$\frac{\partial S_{nw}}{\partial \xi}(\tau,\infty) = 0 \tag{20}$$

where S_{wi} is the irreducible WP saturation at the end of the displacement, and is assumed to be distributed uniformly across the porous medium. The foregoing boundary conditions are suitable for our problem, since all observations and measurements are restricted to a central region of the network, which can be regarded as a piece ("window") of an infinite porous medium.

The total NWP saturation in the porous medium $S_{nwt}(\tau)$ is calculated by

$$S_{nwt}(\tau) = \int_0^1 S_{nw}(\tau,\xi)\,d\xi \tag{21}$$

Likewise, the NWP saturation of a slice of finite thickness extending from ξ_1 to ξ_2 is calculated by

$$S_{nws}(\tau,\xi_m) = \int_{\xi_1}^{\xi_2} S_{nw}(\tau,\xi)\,d\xi \tag{22}$$

where

$$\xi_m = (\xi_1 + \xi_2)/2 \tag{23}$$

For the numerical solution of Eq. 12, coupled with the system of algebraic Eqs. 13–17, the PDAPLUS solver of the commercial software package ATHENA (Stewart and Associates, Inc., Madison, WI) was used, by selecting a finite difference discretization scheme for the space coordinate. The code uses the method of lines to solve mixed systems of nonlinear PDEs and algebraic equations (Caracotsios and Stewart, 1995).

Dimensionless fluid pressures are defined by the relations

$$P_w^* = \frac{P_w}{\Delta P_{nw}^0} \tag{24a}$$

$$P_{nw}^* = \frac{P_{nw}}{\Delta P_{nw}^0} \tag{24b}$$

The local pressure gradient along each phase depends solely on the local NWP saturation $S_{nw}(\tau,\xi)$ and can be obtained by introducing the numerical solution of Eq. 12 into the following relationships

$$\left(-\frac{\partial P_{nw}^*}{\partial \xi}\right) = \frac{\kappa}{\kappa k_{rw} + k_{rnw}}\left[\frac{u_0}{u_c} - k_{rw}\frac{\partial P_c^*}{\partial \xi}\right] \tag{25a}$$

$$\left(-\frac{\partial P_w^*}{\partial \xi}\right) = \frac{\kappa}{\kappa k_{rw} + k_{rnw}}\left[\frac{u_0}{u_c} + \frac{k_{rnw}}{\kappa}\frac{\partial P_c^*}{\partial \xi}\right] \tag{25b}$$

Before the breakthrough of the NWP, the dimensionless total pressure drop across the porous medium ΔP_t^* is equal to the sum of the pressure drop across the NWP, the pressure drop across the WP and the macroscopic capillary pressure at the front, namely

$$\Delta P_t^* = \frac{\Delta P_t}{\Delta P_{nw}^0} = \int_0^{\xi_{cr}}\left(-\frac{\partial P_{nw}^*}{\partial \xi}\right)d\xi + \int_{\xi_{cr}}^1\left(-\frac{\partial P_w^*}{\partial \xi}\right)d\xi + P_c^*(0) \tag{26}$$

where the critical axial distance ξ_{cr} results from the solution of Eq. 12 as the smallest distance satisfying the condition

$$S_{nw}(\tau,\xi_{cr}) \le 10^{-4} \tag{27}$$

For the determination of the NWP breakthrough, it is assumed that a network spanning cluster of the NWP is established, when the NWP saturation at the exit of the porous medium satisfies the condition

$$S_{nw}(\tau,1) \ge 10^{-4} \tag{28}$$

After the breakthrough of NWP, the pressure drop across the porous medium coincides to the pressure drop across the NWP and is given by

$$\Delta P_t^* = \frac{\Delta P_t}{\Delta P_{nw}^0} = \int_0^1\left(-\frac{\partial P_{nw}^*}{\partial \xi}\right)d\xi \tag{29}$$

For the analytical representation of capillary pressure and relative permeability curves, the following simplified Corey type functions

$$P_c = P_c^0\left(1 - \frac{S_{nw}}{1 - S_{wi}}\right)^{-m} \tag{30}$$

$$k_{rw} = k_{rw}^0\left(1 - \frac{S_{nw}}{1 - S_{wi}}\right)^{n} \tag{31}$$

$$k_{rnw} = k_{rnw}^0\left(\frac{S_{nw}}{1 - S_{wi}}\right)^{l} \tag{32}$$

were selected. For primary drainage, the WP end relative permeability $k_{rw}^0 = 1$, while the NWP end relative permeability k_{rnw}^0 can be determined from experimental data and Darcy law by introducing ΔP_{nw}^0 into the relation

$$k_{rnw}^0 = \frac{u_0\,\mu_{nw} L}{k\Delta P_{nw}^0} \tag{33}$$

Therefore, the vector of unknown parameters has four components, namely

$$\boldsymbol{\theta} = \left(P_c^0, m, n, l\right) \tag{34}$$

Parameter estimation

Estimates of the vector $\boldsymbol{\theta}$ were obtained by matching the numerically calculated total NWP saturation, NWP saturation in each of the seven slices, and total pressure drop to corresponding experimental values. The model responses, $S_{nws}(\tau,\xi_m)$, $S_{nwt}(\tau)$, and $\Delta P_t^*(\tau)$ were determined by calculating the integrals of Eqs. 21, 22, 26 and 29 at the experimental values of the independent variables τ and ξ_m, with the Simpson method. For the solution of the nonlinear parameter estimation problem from three-response data, the Bayesian estimator of the GREGPLUS solver of ATHENA software (Stewart et al., 1992) was adapted to the numerical solution of PDAPLUS solver.

For multiresponse data, GREGPLUS computes modal and interval estimates of the parameters using a user-provided matrix of multiresponse observations by using the objective function

$$\Phi(\boldsymbol{\theta}) = \sum_{b=1}^{B} (n_b + m_b + 1) \ln |\boldsymbol{v}_b(\boldsymbol{\theta})| \tag{35}$$

based on a user-selected arrangement of the responses into one or more blocks ($b = 1,\ldots,B$), where n_b and m_b are the number of events and working responses in block b, respectively (Stewart et al., 1992), and $|\boldsymbol{v}_b(\boldsymbol{\theta})|$ is the determinant of the residual matrix defined below. From each block b, GREGPLUS selects m_b working responses whose weighted deviations from the current model, given by $[y_{ij} - f_{ij}(\boldsymbol{\theta})]\sqrt{w_{ij}}$, are linearly independent over the events, where y_{ij}, $f_{ij}(\boldsymbol{\theta})$ and w_{ij} are the observation, model prediction and user-provided weight for response i in event j, respectively. Then, each block sub-matrix function $\boldsymbol{v}_b(\boldsymbol{\theta})$ with elements

$$\boldsymbol{v}_{bik}(\boldsymbol{\theta}) = \sum_{j=1}^{n} \sqrt{w_{ij} w_{kj}} \left[y_{ij} - f_{ij}(\boldsymbol{\theta}) \right] \left[y_{kj} - f_{kj}(\boldsymbol{\theta}) \right] \tag{36}$$

where n is the number of events in the data set, has a positive determinant over the investigated range of $\boldsymbol{\theta}$, as Eq. 35 requires. Note that the dependent variable $\boldsymbol{y}_i$ or $\boldsymbol{f}_i$ represents $S_{nws}(\tau,\xi_m)$, $S_{nwt}(\tau)$, $\Delta P_t^*(\tau)$ for the index values $i = 1, 2, 3$, respectively.

The objective function is expanded as a quadratic function of the parameters, around the initial guesses of the current iteration (Bard, 1974; Stewart et al., 1992). The parametric sensitivities needed for this step can be generated by GREGPLUS with optimized divided-difference steps; alternatively, some or all of them can be provided by the user's subroutine. The resulting minimization problem is solved with successive quadratic programming, starting from the user's guesses for the parameters and using a modified Gauss-Jordan algorithm (Bard, 1974), within a user-defined feasible region; then, a weak line search is conducted to establish an improved objective value and initial parameter vector for the next iteration. Ill-conditioned solutions are avoided by using a threshold value for acceptance of pivotal divisors in the quadratic minimization calculations. Termination of the iteration is controlled by the current quadratic programming predictions of the correction vector. Interval estimates for the individual estimated parameters are then calculated from the final quadratic expansion of the objective functions. Both codes PDAPLUS and GREGPLUS are written in Fortran and are properly incorporated as subroutines in a user-defined code which is written in Athena Visual Workbench (AVW) language and translated automatically to Fortran by ATHENA.

Concepts from Percolation Theory

Finite-size and viscous effects on displacement patterns

At vanishing flow rates, an immiscible displacement process is controlled by capillary forces, and can be modeled as an invasion percolation process (Willemsen, 1984; Wilkinson, 1986). Near the percolation threshold, a percolation quantity X (such as conductivity, percolation probability, and so on) obeys the scaling laws (Stauffer and Aharony, 1992)

$$X \propto \delta^{\alpha/\nu} \tag{37a}$$

$$X \propto w^{\alpha/\nu} \tag{37b}$$

for an infinite lattice and finite lattice of size w (w is dimensionless and coincides to the number of pore lengths per each side of the lattice), respectively, where δ is the correlation length of the system with universal exponent ν, and α is the universal exponent of X. In other words, in finite systems, as the percolation threshold is approached, δ eventually exceeds the lattice size w; thus w becomes the dominant length scale of the system. The percolation probability p defined by

$$p = \int_{r_{\min}}^{\infty} f(r)\,dr \tag{38}$$

expresses the fraction of bonds (pores) that might be invaded by the NWP, if they were all accessible to it, and is equal to the percolation threshold p_{cn} when a network spanning cluster of NWP appears for a first time (Sahimi, 1995). In drainage processes, the finite size of a pore network causes shifts in the percolation threshold (Stauffer and Aharony, 1992) and irreducible wetting phase S_{wi} (Blunt et al., 1992) described by

$$p_{cn}(\infty) - p_{cn}(w) \propto w^{-1/\nu} \tag{39}$$

and

$$S_{wi}(\infty) - S_{wi}(w) \propto w^{-(1+\beta)/\nu} \tag{40}$$

respectively, where β is the universal exponent of the accessibility function (Sahimi, 1995).

Viscous forces introduce an additional finite correlation length δ_v so that viewed on scales less than δ_v the displacement resembles an infinitesimal flow rate, while the effects of viscous forces are evident at scales greater than δ_v (Wilkinson, 1994, 1986; Blunt et al., 1992). An effective correlation length δ_{eff} can then be defined by

$$\frac{1}{\delta_{\text{eff}}} = \frac{1}{\delta_V} + \frac{1}{w} \tag{41}$$

For drainage processes, it has been found that the maximum correlation length that can be developed at a given capillary number (Wilkinson, 1986), scales as

$$\delta_V \propto Ca^{-\nu/(\mu-\beta+1+\nu)} \tag{42}$$

and the NWP saturation is of the order

$$S_{nw} \propto Ca^{\beta/(\mu-\beta+1+\nu)} \tag{43}$$

where μ is the universal exponent of conductivity. Microscopic effects such as the behavior implied by Eqs. 37 can be seen only up to the length scale δ_{eff} which accounts both for finite-size and viscous effects. At very low Ca values, $\delta_V \gg w$, and, hence, $\delta_{\text{eff}} = w$, namely, the network displacement pattern is dominated by a ramified fractal structure governed by finite-size effects on percolation quantities (Eqs. 37b, 39, and 40). At high Ca values, $\delta_V \ll w$, and, hence, $\delta_{\text{eff}} = \delta_V$, namely, the viscous effects become evident at scales smaller than the network size, the network displacement pattern changes, and the percolation pattern, restricted at scales $< \delta_V$, is governed by Eqs. 42 and 43.

A stabilized fully developed displacement consists of a frontal region which moves linearly with time at a frontal velocity u_F, and where the fractal properties of a percolation cluster are valid, and a compact region, where the conventional continuum description is valid (Xu et al., 1998). With the aid of scaling arguments and gradient percolation theory (Yortsos and Xu, 1997; Xu et al., 1998), the following relationship has been found

$$\sigma^{1/(1+\nu)}\left(\sigma^{D-d+\mu/\nu} - b/\kappa\right) \approx \frac{2\Sigma}{Ca_F C} \tag{44}$$

where σ is the front width, d is the topological dimension, D is the mass fractal dimension $(D = d - \beta/\nu)$, Σ is a measure of the variance of the pore-size distribution, C is a constant, and capillary number Ca_F is based on the front velocity $(Ca \propto Ca_F = u_F \mu_{nw}/\gamma)$. In practice, the front width σ coincides to the viscous correlation length, δ_V, namely $\sigma \propto \delta_V$, and for small Ca_F values, Eq. 44 results in the asymptotic relationship (Xu et al., 1998)

$$\sigma \propto \left(\frac{Ca_F C}{2\Sigma}\right)^{-\nu/(1+\mu-\beta+\nu)} \tag{45}$$

which is identical to Eq. 42. The variation of the capillary pressure across the front scales as (Xu et al., 1998)

$$\Delta P_c \propto \sigma^{-1/\nu} \propto Ca^{1/(1+\mu-\beta+\nu)} \tag{46}$$

Near p_{cn}, the relative permeability of NWP scales as (Wilkinson, 1986)

$$k_{rnw} \propto S_{nw}^{\mu/\beta} \tag{47}$$

which in conjunction with Eq. 43 results in

$$k_{rnw} \propto Ca^{\mu/(\mu-\beta+1+\nu)} \tag{48}$$

The NWP saturation within the compact region varies over a length scale $\sigma_c \propto \sqrt{k}\, Ca^{-1}$, and its profile across it can be obtained from the numerical or analytical solution of the averaged macroscopic mass and momentum balances, Eqs. 1 and 2. However, in the frontal region, the NWP saturation profile varies over a length scale σ (Eqs. 44 and 45), and gradient invasion percolation models have been suggested as simulation tools (Hulin et al., 1988; Gouyet et al., 1988; Birovljev et al., 1991; Xu et al., 1988).

Viscous effects on macroscopic parameters

In our approach, the macroscopic two-phase flow equations are used to describe displacements over the compact and frontal regions. In this manner, the aforementioned small-scale viscous effects on the displacement pattern are implicitly introduced into the parameters of capillary pressure and relative permeability curves. By differentiating the macroscopic capillary pressure curve (Eq. 30), we get the asymptotic derivative

$$\left(\frac{dP_c}{dS_{nw}}\right)_{S_{nw}=1-S_{wi}} = \frac{mP_c^0}{1-S_{wi}} \tag{49}$$

From Eqs. 43 and 46, we get the scaling relation

$$\frac{\Delta P_c}{\Delta S_{nw}} \propto Ca^{(1-\beta)/(\mu-\beta+1+\nu)} \tag{50}$$

which in combination with Eq. 49 results in

$$\frac{mP_c^0}{1-S_{wi}} \propto Ca^{(1-\beta)/(\mu-\beta+1+\nu)} \tag{51}$$

Likewise, Eqs. 32 and 48 give the scaling relation

$$k_{rnw}^0 \propto Ca^{\mu/(\mu-\beta+1+\nu)} \tag{52}$$

Equations 43 and 47 yield

$$\frac{dk_{rnw}}{dS_{nw}} \propto S_{nw}^{\mu/\beta-1} \propto Ca^{(\mu-\beta)/(\mu+1-\beta+\nu)} \tag{53}$$

according to Eq. 32, the asymptotic derivative of k_{rnw} at $S_{nw} = 0$ is given by

$$\left(\frac{dk_{rnw}}{dS_{nw}}\right)_{S_{nw}=0} = k_{rnw}^0 l \tag{54}$$

and, from Eqs. 53 and 54, we get

$$k_{rnw}^0 l \propto Ca^{(\mu-\beta)/(\mu+1-\beta+\nu)} \tag{55}$$

The parameter values estimated with history matching can be used to evaluate the validity of the foregoing scaling relations, Eqs. 51, 52 and 55.

Macroscopic Theory for the Nonequilibrium Capillary Pressure

According to the linear thermodynamic theory for the two-phase flow in porous media (Hassanizadeh and Gray, 1993a; Beliaev and Hassanizadeh, 2001; Hassanizadeh et al., 2002), the magnitude of the difference of the (equilibrium) static $P_{c,\text{stat}}$ from the (nonequilibrium) dynamic capillary pressure P_c is proportional to the rate at which drainage takes place, and in dimensionless form can be written as

$$\left(\frac{Ca\gamma}{L\mu_{nw}}\right)\lambda\frac{\partial S_{nwt}}{\partial\tau} = P_c - P_{c,\text{stat}} \tag{56}$$

where the material coefficient λ is non-negative and may still depend on saturation. By applying Eq. 56 to two sets of experimental data, $S_{nwt}(\tau)$ and estimated capillary pressure curves, $P_c(S_{nwt})$, at $Ca = Ca_1$ and $Ca = Ca_2$, and subtracting them from each other to eliminate $P_{c,\text{stat}}$, we get

$$\left(\frac{\gamma}{L\mu_{nw}}\right)\lambda\left[Ca_1\left(\frac{dS_{nwt}}{d\tau}\right)_1 - Ca_2\left(\frac{dS_{nwt}}{d\tau}\right)_2\right] = P_{c,1}(S_{nwt}) - P_{c,2}(S_{nwt}) \tag{57}$$

Results and Discussion

Visualization experiments

Successive shortcuts of displacements for various values of Ca are shown in Figure 4. From the data of Table 2, it has been found that $\langle r_H\rangle = 44.6$ μm and $r_{Hm} = 45.4$ μm (Tsakiroglou, 2002). The number of pore lengths along the axial dimension of the viewed network (Figure 3) was found $N \cong 70$ (Eq. A11). The microscopic capillary number Ca_{L1} and the macroscopic capillary number Ca_{LN} were calculated by using Eqs. A6 and A11, respectively (Table 4). Evidently, $Ca_{L1} \ll 1$ (Table 4), and, hence, at the pore level, the displacement is controlled by capillary forces for the full range of Ca values. This means that scaling concepts of the percolation theory (Wilkinson, 1986; Blunt et al., 1992; Xu et al., 1998) could be used to describe fluid transport over a small length scale depending on Ca (see also below). On the other hand, the network displacement patterns (Figure 4) are controlled by the macroscopic capillary number Ca_{LN}. The viscosity ratio is sufficiently high ($\kappa = 26 \gg 1$) so that, when $Ca_{LN} > 1$ (Table 4), the macroscopic capillary pressure and pressure drop across the displaced WP are negligible compared to the macroscopic pressure drop across the displacing NWP, the displacement is dominated by the frontal drive pattern (Lenormand et al., 1988), and a small amount of WP is trapped in the form of small ganglia (Figures 4a and 4b). When $Ca_{LN} \ll 1$ (Table 4), the macroscopic pressure drop across each phase is negligible compared to the macroscopic capillary pressure, capillarity dominates at the network scale, and a ramified fractal structure appears (this pattern is defined as capillary fingering in Lenormand et al., 1988), whereas a large amount of WP is trapped in the form of ganglia with sizes changing in a broad range (Figures 4d and 4e). Finally, when $Ca_{LN} \approx 1$ (Table 4), the displacement is dominated by a mixture of the aforementioned patterns (Figure 4c).

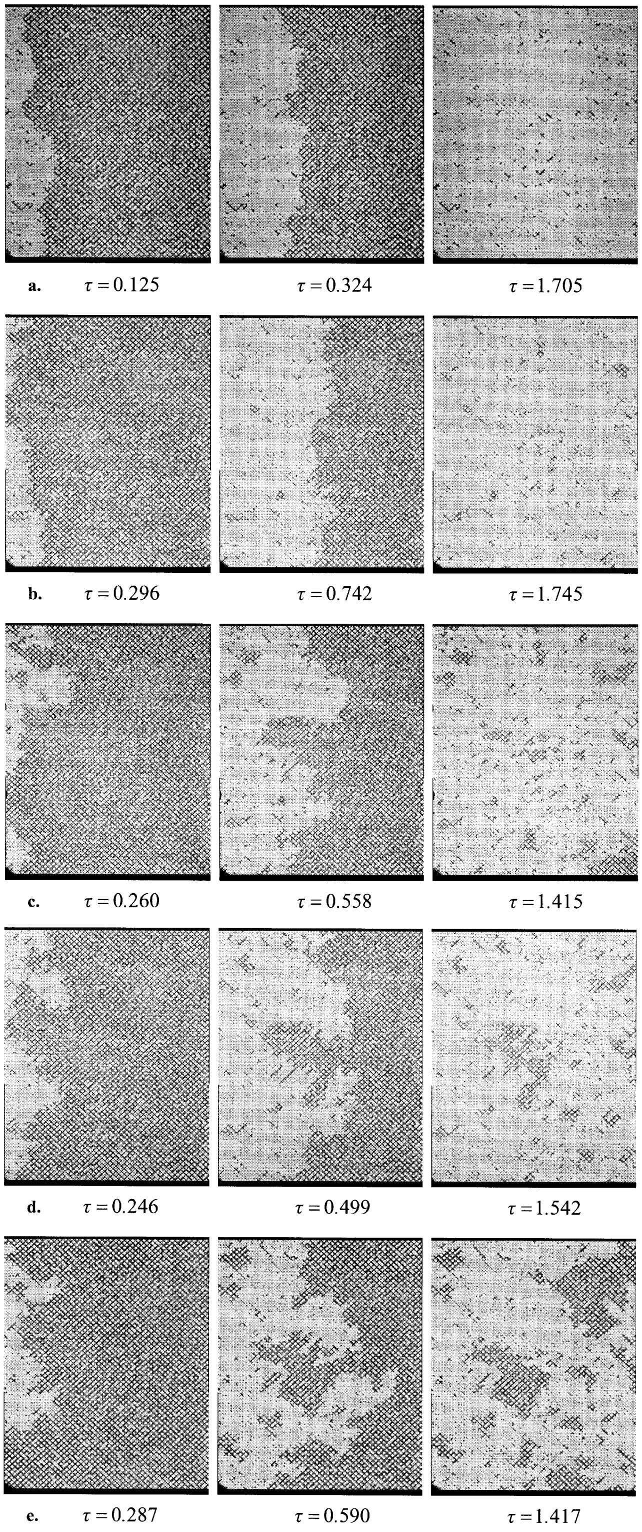
a. $\tau = 0.125$ $\tau = 0.324$ $\tau = 1.705$

b. $\tau = 0.296$ $\tau = 0.742$ $\tau = 1.745$

c. $\tau = 0.260$ $\tau = 0.558$ $\tau = 1.415$

d. $\tau = 0.246$ $\tau = 0.499$ $\tau = 1.542$

e. $\tau = 0.287$ $\tau = 0.590$ $\tau = 1.417$

Figure 4. Successive shortcuts of the displacement of water (dark) by paraffin oil (white) for various values of the capillary number.

(a) $Ca = 1.3\ 10^{-5}$; (b) $Ca = 6.5\ 10^{-6}$; (c) $Ca = 1.3\ 10^{-6}$; (d) $Ca = 1.3\ 10^{-7}$; (e) $Ca = 6.5 \times 10^{-8}$ (the flow direction is from the left to the right).

Table 4. Scale-Dependent Capillary Numbers

Ca	Ca_{L1}	Ca_{LN}
6.55×10^{-8}	0.0002	0.0136
1.31×10^{-7}	0.0004	0.0278
1.31×10^{-6}	0.0040	0.278
6.55×10^{-6}	0.0200	1.405
1.31×10^{-5}	0.0400	2.802

Capillary end effects (Huang and Honarpour, 1998; Toth et al., 2002), arising from the discontinuity of capillary pressure in the wetting phase at the outlet end of the porous sample, may significantly affect the calculated end relative permeabilities and final saturations. In the model porous medium used in experiments (Figure 1b) the fluids enter and expel from the porous medium through small holes connected directly with the pore network. All quantities (pressure drops, saturations) are measured across a central area of the pore network located far from the inlet and outlet ends so that end effects are minimized. Capillary end effects almost vanish even at low Ca values (Figures 4a–4d), and weak nonuniformities of the nonwetting phase saturation across the pore network appear at very low Ca values (Figure 4e).

Estimated nonequilibrium functions

The PDE (Eq. 12) is solved iteratively with the PDAPLUS solver in the time interval $(0,\tau)$ by using a grid refined to 200 discretization points and bounded between $\xi=0$ (left boundary condition, Eq. 19) and $\xi=10$ (right boundary condition, Eq. 20). The parameters of P_c, k_{rw}, k_{rnw} are first estimated for the fastest experimental (Figure 4a), which is a stable displacement with uniform lateral distribution of NWP saturation. These values are introduced then as initial guesses into the parameter estimation problem of the next slower experiment and so on. Modal estimates and intervals of parameters are given in Table 5, whereas the capillary pressure and relative permeability curves are shown in Figures 5 and 6, respectively.

The $P_c(S_{nw})$ increases as the displacement flow rate increases (Figure 5) by tending to an asymptotic function at the highest Ca value (Figure 5). In addition, both $k_{rw}(S_{nw})$ and $k_{rnw}(S_{nw})$ are clearly increasing functions of Ca over the entire range of Ca values (Figure 6). The foregoing experimental results are consistent with theoretical simulations of the unsteady oil/water drainage in pore networks, accounting for the pore scale dynamics (Blunt and King, 1991; Singh and Mohanty, 2003).

Comparative analysis of observed (experimentally measured) data vs. numerical predictions is made in Figures 7–11. The best fit to the observed NWP saturation profile

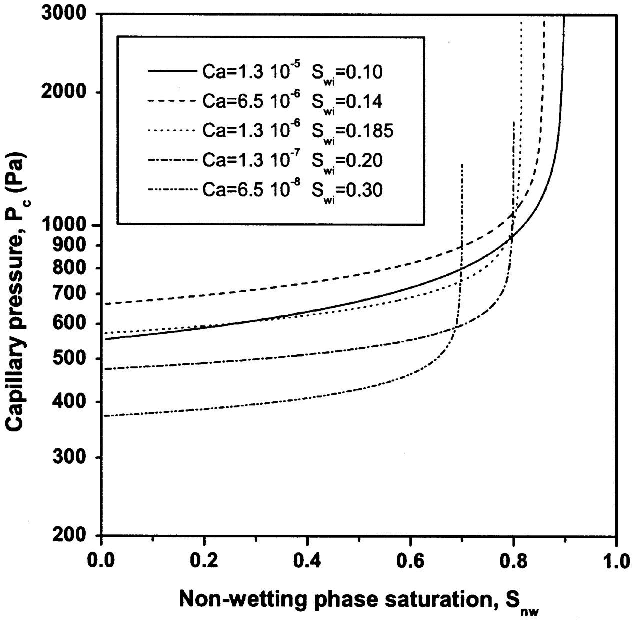

Figure 5. Estimated capillary pressure curves for various values of the capillary number.

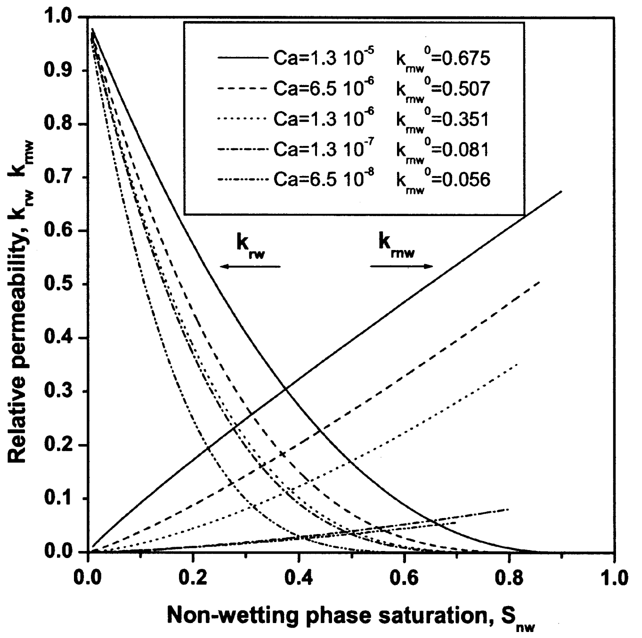

Figure 6. Estimated relative permeability curves for various values of the capillary number.

Table 5. Estimated Parameter Values

Ca	P_c^0 (Pa)	m	n	l
1.3×10^{-5}	553.1 ± 0.25	$0.248\pm2.4\ 10^{-4}$	$2.20\pm1.5\ 10^{-3}$	$0.91\pm6.0\ 10^{-4}$
6.5×10^{-6}	664.1 ± 0.22	$0.181\pm6.8\ 10^{-5}$	$3.02\pm2.3\ 10^{-3}$	$1.20\pm8.1\ 10^{-4}$
1.3×10^{-6}	571.2 ± 0.78	0.142	$3.38\pm2.9\ 10^{-4}$	$1.47\pm2.9\ 10^{-4}$
1.3×10^{-7}	474.6 ± 0.18	$0.112\pm1.7\ 10^{-4}$	$3.45\pm7.8\ 10^{-4}$	$1.51\pm3.5\ 10^{-4}$
6.5×10^{-8}	371.0 ± 13.5	$0.114\pm7.2\ 10^{-3}$	$4.13\pm9.3\ 10^{-2}$	$1.43\pm2.6\times10^{-4}$

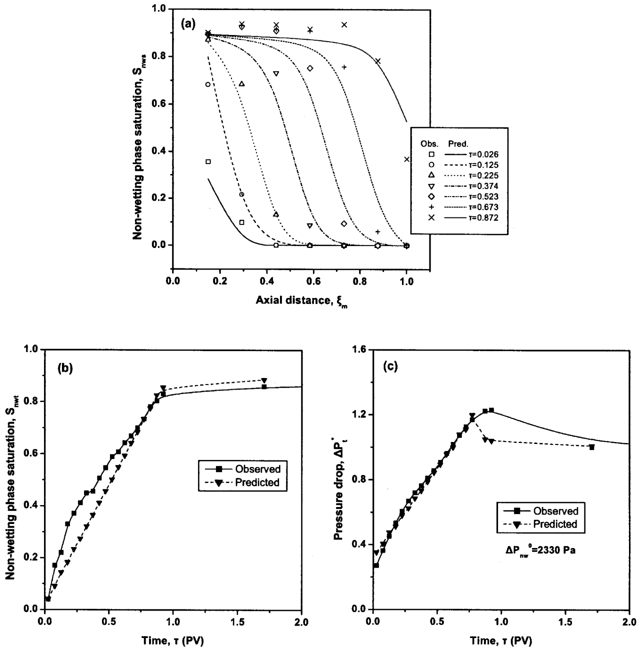

Figure 7. Comparison of experimentally measured with numerically predicted (a) NWP saturation profile, (b) total NWP saturation, and (c) total pressure drop, for $Ca = 1.3\times10^{-5}$ and the parameters values of Table 5.

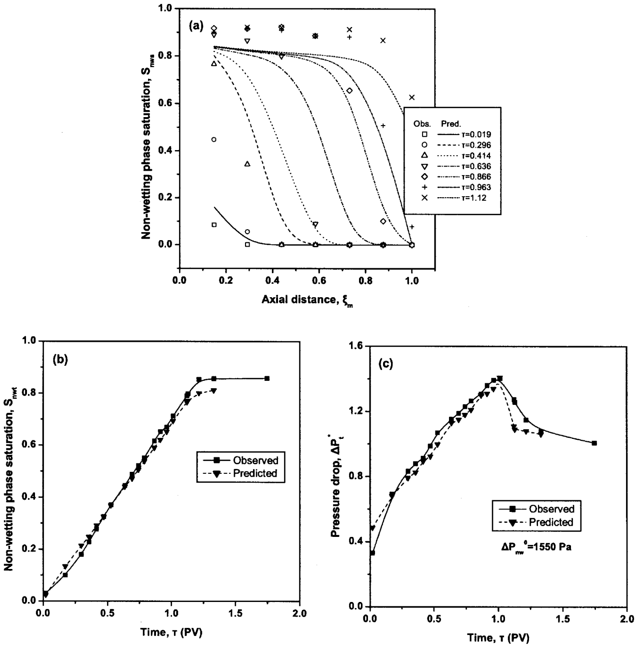

Figure 8. Comparison of experimentally measured with numerically predicted (a) NWP saturation profile, (b) total NWP saturation, and (c) total pressure drop, for $Ca = 6.5\times10^{-6}$ and the parameters values of Table 5.

$S_{nws}(\tau,\xi_m)$ occurs for the fastest experiments (Figures 7a and 8a), where, at the network scale (Table 4), the capillary forces are weak compared to viscous ones, the front width is relatively small, and the resulting frontal drive pattern (Figures 4a and 4b) can successfully be simulated by using the conventional macroscopic equations. In progressively lower *Ca* values, the capillary forces may exceed the viscous ones (Table 4), the front width becomes large compared to the network size (Figures 4c, 4d, and 4e), and the network displacement pattern is gradually dominated by the invasion percolation cluster (Figure 4e). Then, the pattern of the displacement front could be simulated by using a gradient percolation model (Xu et al., 1998), rather than the macroscopic approach adopted here. Subsequently, at low *Ca* values, the discrepancy observed between experimental measurements and numerical predictions of the NWP saturation distribution in the frontal region is reasonable (Figures 10a and 11a). Evidently, changes caused on the displacement pattern by *Ca* and finite network size are implicitly incorporated into the macroscopic parameters of the resulting nonequilibrium capillary pressure and relative permeability curves.

The transient response of the total NWP saturation $S_{nwt}(\tau)$ is predicted satisfactorily almost for all *Ca* values (Figures 7b, 8b, 9b, 10b, and 11b) given that $S_{nwt}(\tau)$ is measured independently of $S_{nws}(\tau,\xi_m)$ and some inconsistency of measured data with mass balance is unavoidable.

Before the NWP breakthrough, the total pressure drop across the viewed region of the pore network (Figures 3 and 4) originates primarily from the pressure drop across the invading viscous NWP and capillary pressure encountered at the displacement front. After the breakthrough of the NWP, the capillary pressure term vanishes and the total pressure drop falls abruptly tending to a constant steady-state value (Figures 7c, 8c, 9c, 10c, and 11c). Near the breakthrough point

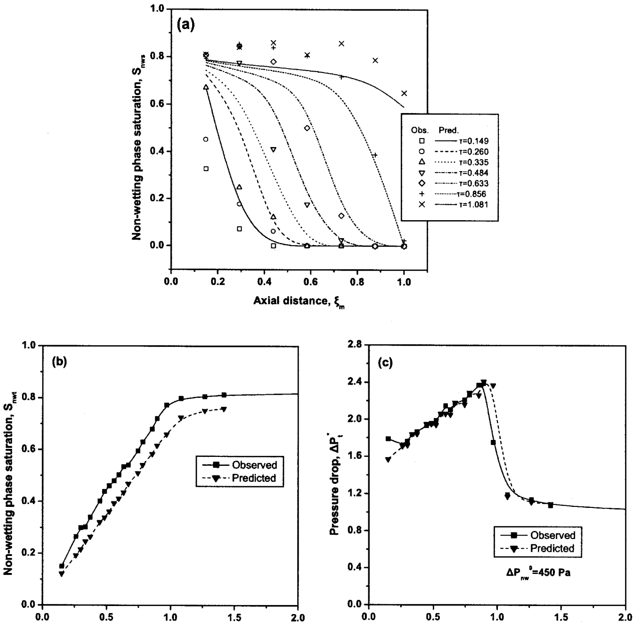

Figure 9. Comparison of experimentally measured with numerically predicted (a) NWP saturation profile, (b) total NWP saturation, and (c) total pressure drop, for $Ca = 1.3\times10^{-6}$ and the parameters values of Table 5.

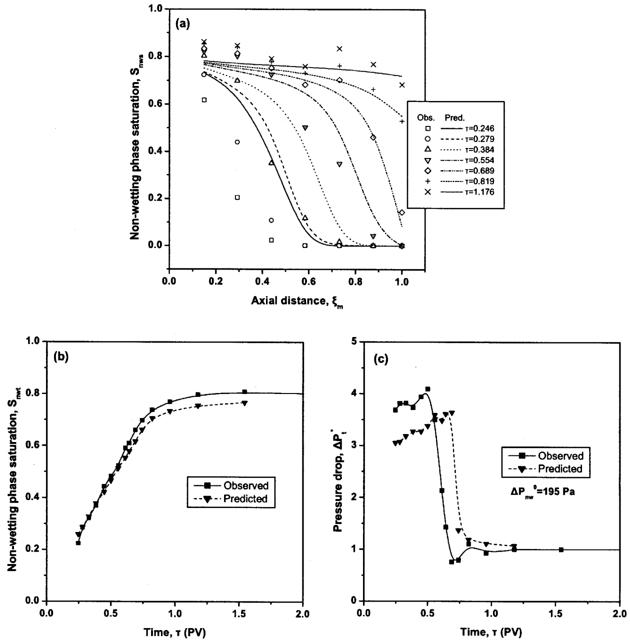

Figure 10. Comparison of experimentally measured with numerically predicted (a) NWP saturation profile, (b) total NWP saturation, and (c) total pressure drop, for $Ca = 1.3 \times 10^{-7}$ and the parameters values of Table 5.

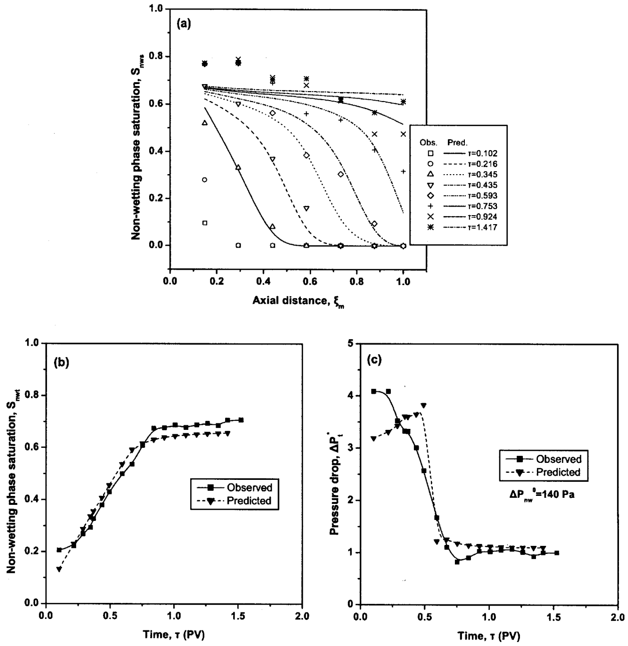

Figure 11. Comparison of experimentally measured with numerically predicted (a) NWP saturation profile, (b) total NWP saturation, and (c) total pressure drop, for $Ca = 6.5 \times 10^{-8}$ and the parameter values of Table 5.

ΔP_t takes on a local maximum, which becomes sharper as Ca decreases and the contribution fraction of $P_c(0)$ to ΔP_t increases (Figures 7c, 8c, 9c, 10c, and 11c). The calculated response of ΔP_t deviates from the experimental one at low Ca values, where the displacement is capillary driven at pore- and network-scale and displacement is dominated by percolation cluster (Figures 4d and 4e).

The values of certain universal scaling exponents for 2-D and 3-D systems are given in Table 6. For 2-D systems, the approximate scaling relations expressed by Eqs. 51, 52, and 55 take the form

$$\frac{mP_c^0}{1-S_{wi}} \propto Ca^{0.246} \tag{58}$$

$$k_{rnw}^0 \propto Ca^{0.37} \tag{59}$$

$$k_{rnw}^0 l \propto Ca^{0.33} \tag{60}$$

The exponents calculated by fitting the estimated parameter values with power laws of the form $y = Ca^{\beta}$ do not differ substantially from the aforementioned universal values (Figures 12a, 12b, and 12c). Hence, the foregoing scaling relations enable us to estimate roughly the functional dependence of the macroscopic parameters of P_c and k_{rnw} on Ca. The discrepancy observed between the exponents of Eqs. 58–60 and those shown in Figure 12 might be attributed to two reasons: (a) lattice finite-size effects on parameter values; (b) asymptotic nature of Eqs. 58–60. It is worthwhile to note that the foregoing analysis and its results with respect to correlations of the macroscopic parameters with Ca are valid, presuming that the displacement is capillary-driven at the pore-scale ($Ca_{L1} \ll 1$).

2-D pore networks could be representative models of the structure of single fractures (Tsakiroglou, 2002). However, the majority of porous media, as, for instance cores of reservoir rocks, should be regarded as large 3-D pore networks with a broad variety in pore sizes (Sahimi, 1995), and unavoidably deviation from the above described behavior is expected. The theoretical analysis must be done carefully so that capillary end effects, arising from the discontinuity of capillarity in the WP at the outlet end of the core, are accounted for. Because of the longer linear dimension L, the length scale of the fully developed flow (compact region) increases significantly, so that the displacement pattern may be dominated by frontal drive even over low Ca values, and finite-size effects on parameter values weaken. On the other hand, the percolation front may also increase substantially because of the high pore size variability (Eq. 45), so that the slope of the capillary pressure curve is expected to increase, and finite-size effects on parameter values strengthen. By replacing the 3-D values

Table 6. Universal Scaling Exponents

Exponent	2-D Systems ($d = 2$)	3-D Systems ($d = 3$)
β	5/36	0.41
ν	4/3	0.88
μ	1.3	2.0
D	91/48	2.53

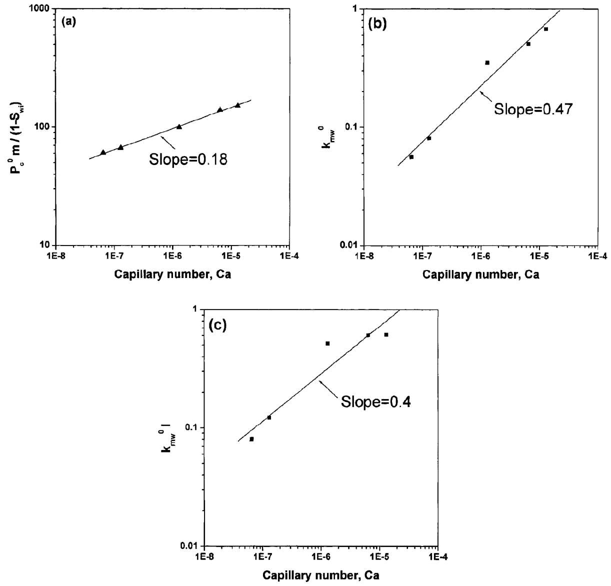

Figure 12. Estimated macroscopic parameters in dependence on *Ca*, (a) $P_c^0 m/(1-S_{wi})$, (b) k_{rnw}^0, (c) $k_{rnw}^0 l$.

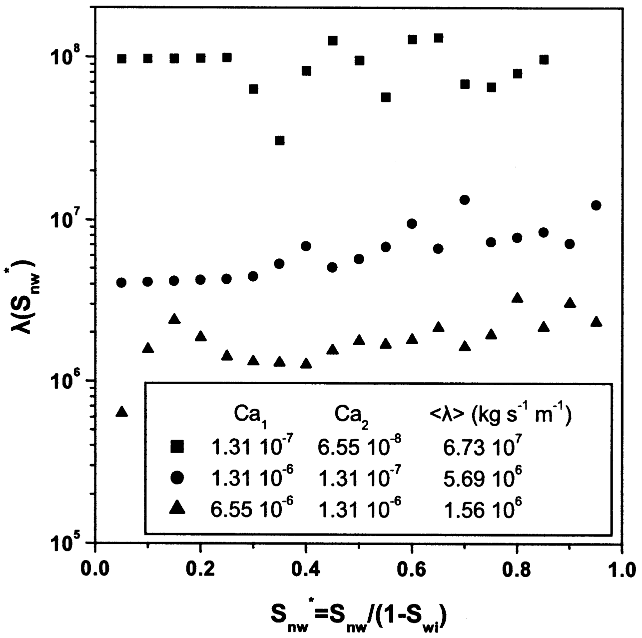

Figure 13. Material coefficient in dependence on the NWP saturation for various values of *Ca*.

of scaling exponents (Table 6) in Eqs. 51, 52, and 55, we get

$$\frac{mP_c^0}{1-S_{wi}} \propto Ca^{0.17} \tag{61}$$

$$k_{rnw}^0 \propto Ca^{0.576} \tag{62}$$

$$k_{rnw}^0 l \propto Ca^{0.45} \tag{63}$$

Equations 61–63 may give us an idea about the dependence of the macroscopic parameters of $P_c(S_{nw})$, $k_{rnw}(S_{nw})$ on *Ca* for 3-D cores. Such relationships might be used to estimate the capillary pressure and relative permeability curves at a *Ca* value when measurements at 1–2 *Ca* values are available. Moreover, the same relationships could be used to evaluate the validity of parameter values estimated from unsteady-state experiments at various *Ca* values.

Experimental data concerning the transient change of the total NWP saturation were used for the determination of the material coefficient λ (Figure 13). Experimental datasets and $P_c(S_{nwt})$ curves corresponding to the two nearest *Ca* values were introduced into Eq. 57. Data points in the vicinity of the irreducible wetting phase saturation S_{wi} (where the slope $dS_{nw}/d\tau$ approaches to zero, and the system tends to equilibrate, Figures 7b–11b) were ignored. The material coefficient was found to change mildly with NWP saturation, and depend strongly on the capillary number range (Figure 13). A mean material coefficient $\langle\lambda\rangle$ was estimated for each pair of *Ca* values with linear fit to Eq. 57 (Figure 13). The material coefficient λ is a capillary damping coefficient and can be regarded as a measure of the speed at which capillary equilibrium is established (Hassanizadeh et al., 2002). Therefore, the higher the capillary number, the smaller the $\langle\lambda\rangle$ value, and the faster the system returns to equilibrium (Figure 13). The calculated values of the material coefficient agree, at least in the order of magnitude, with corresponding ones reported in literature (Hassanizadeh et al., 2002).

Concerning the uniqueness of capillary pressure and relative permeability curves, it is evident that someone can find numerous sets of P_c, k_{rw}, k_{rnw} that may fit to the experimental data satisfactorily. Normally, the final results will depend on the (a) quality of data, (b) number of datasets, (c) adequacy of the two-phase flow equations and P_c, k_{rw}, k_{rnw} models, and (d) efficiency of the computational technique. In the present work, we attempt to maximize (a), (b) and (d) by using conventional two-phase flow equations and P_c, k_{rw}, k_{rnw} models, and, assuming that at the scale of the pore network, the capillary pressure and relative permeability functions depend on the global rather than the local flow rates. Likewise, at the core scale, the dependence of the relative permeability and capillary pressure curves on the local capillary number (which changes with time and spatial coordinate from 0 to *Ca*) may be ignored so that the classical fractional flow equations are used. However, at the reservoir scale, the *Ca* dependent P_c, k_{rw}, k_{rnw} curves (determined as described above from unsteady-state experiments performed on representative cores at several *Ca* values) may be regarded, at each point of the numerical grid, as functions of the local fractional flow of the NWP (Tsakiroglou et al., 1998), namely

$$k_{rw} = k_{rw}(S_{nw}, F_{nw}),\ k_{rnw} = k_{rnw}(S_{nw}, F_{nw}),$$
$$P_c = P_c(S_{nw}, F_{nw}) \tag{64}$$

In this manner, additional nonlinearities are introduced into the fractional flow Eqs. 7 and 8, and elaborate computational methods are required for their numerical solution. A two-scale approach of this type enables us to account for small-scale (core-scale) viscous effects on the simulated saturation profiles at the reservoir scale.

Conclusions

Drainage experiments of the immiscible displacement of an aqueous wetting phase (water) by an oleic nonwetting phase (paraffin oil) are performed on a planar glass-etched pore network, under constant viscosity ratio, and varying values of the capillary number. The measured transient changes of the axial NWP saturation distribution, total NWP saturation, and total pressure drop are used for the parameter estimation of the Corey type capillary pressure and relative permeability functions with history matching. The mathematical model consists of the conventional equations describing the 1-D macroscopic flow of two fluids in an isotropic and homogeneous porous medium. In history matching, the ATHENA software package is utilized, where the mixed system of nonlinear partial differential and algebraic equations is solved with the PDAPLUS solver and the optimal parameter values are estimated by using the Bayesian estimator of the GREG-PLUS solver. Gradient percolation theory allows the derivation of approximate scaling laws describing the variation of macroscopic parameters with the capillary number in terms of universal scaling exponents. The estimated capillary pressure curves at varying values of the capillary number are used to determine the material coefficient of the thermodynamic theory of capillary pressure (Hassanizadeh et al., 2002).

The most important conclusions are outlined below.

- At the pore scale, the displacement is capillary-driven, while, at the network scale, the displacement may be governed by capillary or viscous forces depending on capillary number and pore network size.
- The $P_c(S_{nw})$, $k_{rnw}(S_{nw})$, $k_{rw}(S_{nw})$ curves are increasing functions of the capillary number in agreement with earlier simulations with dynamic pore network simulators.
- The estimated capillary pressure and relative permeability functions are sensitive to the dominant transient displacement pattern, which, at the network-scale, changes gradually fron the invasion percolation cluster to the frontal drive, as the capillary number increases.
- The displacement pattern consists of a compact region, where the macroscopic equations are applicable, and a ramified frontal region that can be described by a viscous gradient percolation model; the width of the frontal region is an increasing function of the capillary number and may be comparable to the pore network size at low *Ca* values.
- Scaling laws arising from the gradient percolation theory fit satisfactorily to parameter values estimated by matching experimental data with the macroscopic two-phase flow equations; such relationships can be used as a guide to evaluate estimated macroscopic parameters of $P_c(S_{nw})$, $k_{rnw}(S_{nw})$, $k_{rw}(S_{nw})$.
- Regarding the variation of $P_c(S_{nw})$, $k_{rnw}(S_{nw})$, $k_{rw}(S_{nw})$ with *Ca*, differences between 2-D and 3-D porous media are associated with universal scaling exponents depending exclusively on dimensionality, lattice size, and pore-size variability.
- The material coefficient is a decreasing function of the capillary number, and such a behavior should be taken into account in applying the macroscopic thermodynamic theory (Hassanizadeh and Gray, 1993a) to transient two-phase flow processes.
- Rate-dependent $P_c(S_{nw}$, $k_{rnw}(S_{nw})$, $k_{rw}(S_{nw})$ curves estimated from core experiments can be coupled with the macroscopic two-phase flow equations in order to account for small-scale viscous effects on simulations at the reservoir scale.

Acknowledgments

This work was performed under Energy Environment and Sustainable Development (EESD) contract number EVK1-CT1999-00013 (project acronym: TRACe-Fracture) supported by the European Commission.

Literature Cited

Aker, E., K. J. Maloy, A. Hansen, and G. G. Batrouni, "A Two-Dimensional Network Simulator for Two-Phase Flow in Porous Media," *Transp. Porous Media*, **32**, 163 (1998).

Akin, S., "Estimation of Fracture Relative Permeabilities from Unsteady State Corefloods," *J. Pet. Sci. Eng.*, **30**, 1 (2001).

Akin, S., and B. Demiral, "Genetic Algorithm for Estimating Multiphase Flow Functions from Unsteady-State Displacement Experiments," *Comput. & Geosciences*, **24**, 251 (1998).

Avraam, D. G., and A. C. Payatakes, "Flow Regimes and Relative Permeabilities during Steady-State Two-Phase Flow in Porous Media," *J. Fluid Mech.*, **293**, 207 (1995a).

Avraam, D. G., and A. C. Payatakes, "Generalized Relative Permeability Coefficients during Steady-State Two-Phase Flow in Porous Media and Correlation with the Flow Mechanisms," *Transp. Porous Media*, **20**, 135 (1995b).

Bard, Y., *Nonlinear Parameter Estimation*, Academic Press, London (1974).

Bear, J., *Dynamics of Fluids in Porous Media*, Elsevier, New York (1972).

Beliaev, A. Y., and S. M. Hassanizadeh, "A Theoretical Model of Hysteresis and Dynamic Effects in the Capillary Relation for Two-Phase Flow in Porous Media," *Transp. Porous Media*, **43**, 487 (2001).

Bentsen, R. G., and A. A. Manai, "On the Use of Conventional Cocurrent and Countercurrent Effective Permeabilities to Estimate the Four Generalized Permeability Coefficients which Arise in Coupled, Two-Phase Flow," *Transp. Porous Media*, **11**, 243 (1993).

Birovljev, A., L. Furuberg, J. Feder, T. Jossang, K. J. Maloy, and A. Aharony, "Gravity Invasion Percolation in Two Dimensions: Experiment and Simulation," *Phys. Rev. Lett.*, **67**, 584 (1991).

Blunt, M., and P. King, "Relative Permeabilities from Two- and Three-Dimensional Pore-Scale Network Modeling," *Transp. Porous Media*, **6**, 407 (1991).

Blunt, M., M. J. King, and H. Scher, "Simulation and Theory of Two-Phase Flow in Porous Media," *Phys. Rev. A*, **46**, 7680 (1992).

Caracotsios, M., and W. E. Stewart, "Sensitivity Analysis of Initial-Boundary-Value Problems with Mixed PDEs and Algebraic Equation; Applications to Chemical and Biochemical Systems," *Comput. Chem. Eng.*, **19**, 1019 (1995).

Chardaire-Riviere, C., G. Chavent, J. Jaffre, J. Liu, and B. J. Bourbiaux, "Simultaneous Estimation of Relative Permeabilities and Capillary Pressure," *SPE Form. Eval.*, 283 (Dec. 1992).

Constantinides, G. N., and A. C. Payatakes, "Network Simulation of Steady-State Two-Phase Flow in Consolidated Porous Media," *AIChE J.*, **42**, 369 (1996).

Dullien, F. A. L., and M. Dong, "Experimental Determination of the Flow Transport Coefficients in the Coupled Equations of Two-Phase Flow in Porous Media," *Transp. Porous Media*, **25**, 97 (1996).

Fourar, M., S. Bories, R. Lenormand, and P. Persoff, "Two-Phase Flow in Smooth and Rough Fractures: Measurement and Correlation by Porous-Medium and Pipe Flow Models," *Water Resour. Res.*, **29**, 3699 (1993).

Goode, P. A., and T. S. Ramakrishnan, "Momentum Transfer across Fluid-Fluid Interfaces in Porous Media: a Network Model," *AIChE J.*, **39**, 1124 (1993).

Hassanizadeh, S. M., and W. G. Gray, “Thermodynamic Basis of Capillary Pressure in Porous Media,” *Water Resour. Res.*, **29**, 3389-3405 (1993a).

Hassanizadeh, S. M., and W. G. Gray, “Toward an Improved Description of the Physics of Two-Phase Flow,” *Adv. Water Resour.*, **16**, 53 (1993b).

Hassanizadeh, S. M., M. A. Celia, and H. K. Dahle, “Dynamic Effect in the Capillary Pressure-Saturation Relationship and its Impacts on Unsaturated Flow,” *Vadoze Zone J.*, **1**, 38 (2002).

Heaviside, J., “Measurement of Relative Permeability,” *Interfacial Phenomena in Petroleum Recovery*, N. R. Morrow, ed., pp. 377–411, Marcel-Dekker, New York (1991).

Huang, D. D., and M. M. Honarpour, “Capillary End Effects in Coreflood Calculations,” *J. Pet. Sci. Eng.*, **19**, 103 (1998).

Hughes, R. G., and M. J. Blunt, “Pore Scale Modeling of Rate Effects in Imbibition,” *Transp. Porous Media*, **40**, 295 (2000).

Hulin, J. P., E. Clement, and C. Baudet, “Quantitative Analysis of an Invading-Fluid Invasion Front under Gravity,” *Phys. Rev. Lett.*, **61**, 333 (1988).

Gouyet, J.-F., M. Rosso, and B. Sapoval, “Fractal Structure of Diffusion and Invasion Fronts in Three-Dimensional Lattices through the Gradient Percolation Approach,” *Phys. Rev. B*, **37**, 1832 (1988).

Jennings, J. W., D. S. McGregor, and R. A. Morso, “Simultaneous Determination of Capillary Pressure and Relative Permeability by Automatic History Matching,” *SPE Form. Eval.*, 322 (June 1988).

Johnson, E. F., D. P. Bossler, and V. O. Naumann, “Calculation of Relative Permeability from Displacement Experiments,” *J. Pet. Tech.*, **61** (June 1959).

Johnson, V. M., and L. L. Rogers, “Applying Soft Computing Methods to Improve the Computational Tractability of a Subsurface Simulation–Optimization Problem,” *J. Pet. Sci. Eng.*, **29**, 153 (2001).

Kalaydjian, F., “Origin and Quantification of Coupling between Relative Permeabilities for Two-Phase Flow in Porous Media,” *Transp. Porous Media*, **5**, 215 (1990).

Kantzas, A., and I. Chatzis, “Network Simulation of Relative Permeability Curves using a Bond Correlated-Site Percolation Model of Pore Structure,” *Chem. Eng. Commun.*, **69**, 191 (1988).

Knackstedt, M. A., A. P. Sheppard, and M. Sahimi, “Pore Network Modelling of Two-Phase Flow in Porous Rock: the Effect of Correlated Heterogeneity,” *Adv. Water Resour.*, **24**, 257 (2001).

Kulkarni, R., A. T. Watson, J.-E. Norttvedt, and A. Sylte, “Two-Phase Flow in Porous Media: Property Identification and Model Validation,” *AIChE J.*, **44**, 2337 (1998).

Lenormand, R., E. Touboul, and C. Zarcone, “Numerical Models and Experiments on Immiscible Displacement in Porous Media,” *J. Fluid Mech.*, **189**, 165 (1988).

Levine, S., and D. L. Cuthiel, “Relative Permeabilities in Two-Phase Flow through Porous Media: an Application of Effective Medium Theory,” *J. Can. Pet. Tech.*, **25**, 74 (1986).

Mejia, G. M., K. K. Mohanty, and A. T. Watson, “Use of in situ Situation Data in Estimation of Two-Phase Flow Functions in Porous Media,” *J. Pet. Sci. Eng.*, **12**, 233 (1995).

Mitlin, V., B. Lawton, and L. Owen, “A Semi-analytical Procedure for Estimating Relative Permeability from Displacement Experiments: Account for Pre-Breakthrough Data,” *Int. J. Eng. Sci.*, **37**, 1051 (1999).

Persoff, P., and K. Pruess, “Two-Phase Flow Visualization and Relative Permeability Measurement in Natural Rough-Walled Rock Fractures,” *Water Resour. Res.*, **31**, 1175 (1995).

Sahimi, M., *Flow and Transport in Porous Media and Fractured Rock: From Classical Methods to Modern Approaches*, VCH, Weinheim, Germany (1995).

Savioli, G. B., and M. S. Bidner, “Comparison of Optimization Techniques for Automatic History Matching,” *J. Pet. Sci. Eng.*, **12**, 25 (1994).

Scheidegger, A. E., *The Physics of Flow through Porous Media*, Univ. of Toronto, Toronto (1974).

Sigmund, P., and F. McCaffery, “An Improved Unsteady-State Procedure for Determining the Relative Permeability Characteristics of Heterogeneous Media,” *SPE J.*, **169**, 15 (1979).

Singh, M., V. Mani, M. M. Honarpour, and K. K. Mohanty, “Comparison of Viscous and Gravity Dominated Gas-Oil Relative Permeabilities,” *J. Pet. Sci. Eng.*, **30**, 67 (2001).

Singh, M., and K. K. Mohanty, “Dynamic Modelling of Drainage through Three-Dimensional Porous Materials,” *Chem. Eng. Sci.*, **58**, 1 (2003).

Stauffer, D., and A. Aharony, *Introduction to Percolation Theory*, Taylor & Francis, London (1992).

Stewart, W. E., M. Caracotsios, and J. P. Sorensen, “Parameter Estimation from Multiresponse Data,” *AIChE J.*, **38**, 641 (1992).

Tao, T. M., and A. T. Watson, “Accuracy of JBN Estimates of Relative Permeability: Part 1—Error Analysis,” *Soc. Pet. Eng. J.*, 209 (Apr. 1984).

Theodoropoulou, M., V. Karoutsos, and C. Tsakiroglou, “Investigation of the Contamination of Fractured Formations by Non-Newtonian Oil Pollutants,” *J. Environm. Forensics*, **2**, 321 (2001).

Toth, J., T. Bodi, P. Szucs, and F. Civan, “Convenient Formulae for Determination of Relative Permeability from Unsteady-State Fluid Displacements in Core Plugs,” *J. Pet. Sci. Eng.*, **36**, 33 (2002).

Tsakiroglou, C. D., “A Methodology for the Derivation of non-Darcian Models for the Flow of Generalized Newtonian Fluids in Porous Media,” *J. Non-Newtonian Fluid Mech.*, **105**, 79 (2002).

Tsakiroglou, C. D., D. G. Avraam, and A. C. Payatakes, “Improved Macroscopic Equations of Two-Phase Flow in Porous Media Based on New Models of the Capillary Pressure and Relative Permeability,” *Proc. of the XII Int. Conf. on Computational Methods in Water Resources*, Crete, V. N. Burganos et al., eds., **2**, Computational Mechanics Publications, Southampton, U.K., 27 (June 15–19, 1998).

Vizika, O., D. G. Avraam, and A. C. Payatakes, “On the Role of the Viscosity Ratio during Low-Capillary Number Forced Imbibition in Porous Media,” *J. Colloid Interface Sci.*, **165**, 386 (1994).

Vizika, O., and A. C. Payatakes, “Parametric Experimental Study of Forced Imbibition in Porous Media,” *PhysicoChem. Hydrodyn.*, **11**, 187 (1989).

Watson, A. T., P. D. Kerig, P. C. Richmond, and T. M. Tao, “An Improved Method for Estimating Relative Permeabilities from Displacement Experiments,” *Proc. of the 56th California Regional Meeting of the SPE*, Paper SPE 15064, Oakland, CA, Society of Petroleum Engineers, Richardson, TX, 165 (Apr. 2–4, 1986).

Whitaker, S., “Flow in Porous Media II: The Governing Equations for Immiscible, Two-Phase Flow,” *Transp. Porous Media*, **1**, 105 (1986).

Wilkinson, D., “Percolation Model of Immiscible Displacement in the Presence of Buoyancy Forces,” *Phys. Rev. A*, **30**, 520 (1984).

Wilkinson, D., “Percolation Effects in Immiscible Displacement,” *Phys. Rev. A*, **34**, 1380 (1986).

Willemsen, J. F., “Investigations on Scaling and Hyperscaling for Invasion Percolation,” *Phys. Rev. Lett.*, **52**, 2197 (1984).

Xu, B., Y. C. Yortsos, and D. Salin, “Invasion Percolation with Viscous Forces,” *Phys. Rev. E.*, **57**, 739 (1998).

Yortsos, Y. C., and B. Xu, “Phase Drainage of Fully Developed Drainage in Porous Media,” *Phys. Rev. Lett.*, **79**, 4581 (1997).

Appendix

In order to relate the pore structure characteristics with the macroscopic flow pattern, we define the pore-scale capillary number Ca_{L1}, as the ratio of the pressure drop across a single pore ΔP_{V1} to the capillary pressure P_{C1}, required for the filling of a pore with NWP. The equivalent hydraulic radius r_H is defined as the ratio of the area to the perimeter of the cross-section, and the pore aspect ratio ρ is defined as the ratio of the pore depth to width. An effective hydraulic radius r_{Hm} can be calculated by considering a mean aspect ratio $\langle \rho \rangle = \langle W_p \rangle / \langle D_p \rangle$, and averaging r_H over the pore network with the aid of the effective medium theory (Tsakiroglou, 2002). Then, the pressure drop for the flow of NWP through an elliptical pore of the effective network, at an average (intrinsic) velocity $u_P = u_0/\phi$ is given by

$$\Delta P_{V1} = \frac{\mu_{nw} L_P \pi^2 \left(1 + \langle \rho \rangle^2\right) u}{4E^2 r_{Hm}^2 \phi} = \frac{\mu_{nw} L_P u}{k} \qquad \text{(A1)}$$

where E is an elliptical integral of second kind, defined by

$$E\left(\sqrt{1-\langle \rho\rangle^2},\pi/2\right)=\int_0^{\pi/2}\sqrt{1-\left(1-\langle \rho\rangle^2\right)\sin^2\theta}\,d\theta \tag{A2}$$

ϕ is the porosity, defined by

$$\phi=\frac{\pi\langle D_P\rangle\langle W_P\rangle}{4L_P^2} \tag{A3}$$

and u_0 is the average (superficial) flow velocity of NWP ($u_0 = q_0/A_P$), where A_P is an apparent cross-section area

$$A_P=W_T L_P \tag{A4}$$

The capillary pressure at equilibrium is given by

$$P_{C1}=\frac{\gamma\cos\omega}{r_{Hm}} \tag{A5}$$

where ω is the (static) receding contact angle for the investigated fluid/solid system. Given that $\cos\omega = O(1)$, this factor can be neglected and Ca_{L1} is written

$$Ca_{L1}=\frac{\Delta P_{V1}}{P_{C1}}\cong\frac{\pi^3\langle \rho\rangle\left(1+\langle \rho\rangle^2\right)}{64E^4}\left(\frac{L_p}{r_{Hm}}\right)^3 Ca=\left(\frac{L_P r_{Hm}}{k}\right)Ca \tag{A6}$$

where the global capillary number Ca is given by

$$Ca=\frac{u_0\,\mu_{nw}}{\gamma} \tag{A7}$$

The pressure drop in the NWP, across a network length $L = NL_P$ is given by

$$\Delta P_{VN}=\frac{u_{nw}\,\mu_{nw}NL_P}{kk_{rnw}} \tag{A8}$$

The corresponding macroscopic capillary pressure at equilibrium P_{CN} can be obtained by averaging the interfacial curvatures over the total interfacial area of the pore network (Whitaker, 1986). However, for an analysis of the order of magnitude, it can be approximated as $P_{CN} \cong P_{C1}$. It is $k_{rnw} \propto S_{nw}^l$, and, therefore, the macroscopic network-scale capillary number is given by

$$Ca_{LN}=\frac{\Delta P_{VN}}{P_{CN}}\cong\frac{r_{Hm}L_P N}{kk_{rnw}}Ca \tag{A9}$$

By assuming that, $k_{rnw} = O(1)$, Eq. A9 is finally simplified to

$$Ca_{LN}\approx NCa_{L1} \tag{A10}$$

Note that the number of pore lengths N along one dimension L of the pore network is approximated by the relation

$$N=\frac{L}{L_P\cos\theta} \tag{A11}$$

where θ is the angle formed between the main flow direction and the pore axis.

Manuscript received Sept. 11, 2002, revision received Feb. 11, 2003, and final revision received May 16, 2003.